AIP | The Journal of Chemical Physics

Spectroscopic observation of gold-dicarbide: Photodetachment and velocity map imaging of the AuC2 anion

Bradley R. Visser, Matthew A. Addicoat, Jason R. Gascooke, Warren D. Lawrance, and Gregory F. Metha

Citation: The Journal of Chemical Physics **138**, 174310 (2013); doi: 10.1063/1.4803465
View online: http://dx.doi.org/10.1063/1.4803465
View Table of Contents: http://scitation.aip.org/content/aip/journal/jcp/138/17?ver=pdfcov
Published by the AIP Publishing

Spectroscopic observation of gold-dicarbide: Photodetachment and velocity map imaging of the AuC_2 anion

Bradley R. Visser,[1,a)] Matthew A. Addicoat,[2] Jason R. Gascooke,[3] Warren D. Lawrance,[3] and Gregory F. Metha[1,b)]

[1]*Department of Chemistry, University of Adelaide, South Australia 5005, Australia*
[2]*Department of Chemistry, Nagoya University, Nagoya 464-8602, Japan*
[3]*School of Chemical and Physical Sciences, Flinders University, G.P.O. Box 2100, Adelaide, South Australia 5001, Australia*

(Received 23 November 2012; accepted 17 April 2013; published online 7 May 2013)

Photoelectron spectra following photodetachment of the gold dicarbide anion, AuC_2^-, have been recorded using the velocity map imaging technique at several excitation wavelengths. The binding energy spectra show well-defined vibrational structure which, with the aid of computational calculations and Franck-Condon simulations, was assigned to a progression in the Au–C stretching mode, ν_3. The experimental data indicate that the features in the spectrum correspond to a $^2\mathbf{A}' \leftarrow {}^3\mathbf{A}'$ transition, involving states which we calculate to have bond angles ∼147° but with a low barrier to linearity. © *2013 AIP Publishing LLC*. [http://dx.doi.org/10.1063/1.4803465]

I. INTRODUCTION

Small metal carbides provide an interesting starting point to understanding growth mechanisms of the various metal-carbon nanomaterials.[1–8] In this context, Wang and co-workers[9–12] explored the structure and bonding in a range of neutral metal-dicarbide (M–C_2) species, accessed from the anion via electron photodetachment. The metals studied have included scandium,[9] titanium,[10] vanadium,[9,13] chromium,[9,13,14] manganese,[9] iron,[9,12,13] and cobalt.[9,13] The M–C_2 structure was identified as involving side-bonding of the metal to the C_2 entity in a T-shaped configuration with C_{2v} symmetry in all cases.

In contrast to the ubiquitous T-shaped C_{2v} geometry for the metals identified above, Cohen *et al.*[15] have calculated a Au–C–C connected configuration for AuC_2 as part of a study of small gold-carbon clusters accessed by fullerene ion impact on a gold target. In view of the predicted deviation from a C_{2v} geometry on the part of AuC_2, we have undertaken an exploration of this species using photodetachment electron imaging to investigate the structure of the neutral species.

Photoelectron spectroscopy (PES) of anions is a popular technique for determining the electronic and, ideally, the vibrational structure of the corresponding neutral species. Electron imaging is a recently developed form of photoelectron spectroscopy that provides spectral information that is very similar to that obtained by conventional PES. Good spectral resolution is achieved in the imaging approach using the technique of velocity map imaging (VMI) developed by Eppink and Parker.[16] The use of velocity map photoelectron imaging has two main advantages over photoelectron spectroscopy. First, the detection efficiency is independent of electron kinetic energy, unlike traditional PES which suffers from low detection efficiencies at low electron kinetic energy. Second, the full three-dimensional (3D) photodetachment distribution is detected in the form of a two-dimensional (2D) projection, from which the original 3D distribution can be reconstructed. Extraction of the central portion of the 3D projection (e.g., containing only electrons that have detachment velocities purely parallel to the detector plane) allows simultaneous measurement of the electron kinetic energy distribution and the electron angular distribution, thus returning additional information on the photodetachment process. The only significant drawback of the velocity map imaging method is the relative complexity of the post-processing of the data compared to conventional PES.

Few investigations of transition metal clusters with the VMI technique have been reported. In 2010, Wu *et al.*[17] showed velocity map images of Au, Au_2, and the monohydrides of these species. These species had been studied previously by conventional photoelectron (Au and Au_2,[18] and Au_nH[19]) and infrared spectroscopy[20,21] and thus the study primarily acted as a proof of principle of the velocity map imaging technique for transition metal cluster species. Vibrationally resolved spectra were obtained for the AuH and Au_2H species, thus demonstrating the usefulness of the technique. MI_2 species (M = Cs, Cu, and Au) have also been investigated using VMI by Wang *et al.*,[22] also in 2010. The images of AuI_2 and CuI_2 gave well-defined vibrational structure and thus could be examined at a high level of detail. Through comparison with calculation, the nature of the chemical bonding was found to be ionic in CsI_2 and strongly covalent in AuI_2.

Gas phase AuC_2 is relatively unknown and the few data that exist are summarised as follows. Duncan and co-workers[23] studied metal carbide cluster cations, $M_nC_m^+$ (n = 1–2), of gold and copper and subsequent photodissociation at 355 nm. A reduced ion intensity was observed for gold-carbide cluster stoichiometries immediately

a)Present address: Lehrstuhl für Physicalische Chemie I, Technische Universität München, Garching 85747, Germany.
b)Author to whom correspondence should be addressed. Electronic mail: greg.metha@adelaide.edu.au. Telephone: +61 8 8313 5943. Fax: +61 8 8313 4358.

after $m = 3$, 6, 9, and 12. The fragmentation patterns of size-selected $Au_nC_m^+$ clusters were found to be size dependent, with clusters containing an even number of carbon atoms primarily losing C_3 and large odd clusters losing a neutral Au atom. Specifically, AuC_2^+ was observed to be formed in relatively low concentrations and no photodissociation data were obtained. Density functional theory (DFT) calculations were only performed for the neutral and cationic CuC_{3-11} clusters, and these showed the lowest energy structures to be linear singlet states for all cations except for the cyclic CuC_{10}^+.

As mentioned above, Cohen *et al.*[15] studied the products arising from fullerene ions impacting a metal surface at keV energies. A wide variety of small metal carbide clusters were observed including both cationic and anionic Au_nC_m ($n = 1$–5, $m = 1$–10, 12) clusters, the latter being very intense. Both the cationic and anionic clusters showed an odd-even variation in ion intensity (even m being more abundant). These workers also performed DFT calculations (using MPW1PW91/SDD) that predicted the lowest energy geometries for AuC_{1-7}^+ clusters to be linear with alternating multiplicities (i.e., AuC^+ is singlet, AuC_2^+ is triplet, etc.). The lowest energy structure of the AuC_2^+ cation was calculated to be a bent ($\angle_{Au-C-C} = 160^\circ$) triplet state when using the B3LYP/LANL2DZ combination.

II. EXPERIMENTAL METHOD

Since the specific apparatus used for these experiments has not been previously published, a detailed description is given here. Experiments were performed under high vacuum conditions within a two chamber, differentially pumped system operated at pressures of 1×10^{-4} and 1×10^{-6} mbar, respectively. Gold-carbide clusters were produced within a Smalley-type laser ablation source modelled on our existing designs.[24] The source was operated with benzene seeded in helium gas to produce the metal-carbon products. The clusters exit the source and expand towards a two stage Wiley-McLaren type time of flight where anion species are pulse extracted orthogonally into a drift region. Ion optics corrects the flight path of the extracted anions so that they enter the VMI electrodes positioned immediately after the drift region. The geometry of the time of flight electrodes was designed such that the second order space focus was coincident with the photodetachment point within the VMI electrodes.[25] At this point, the ion packets of the clusters were condensed to small volumes and separated in time according to their mass to charge ratio, m/e. Individual m/e species are probed by varying the photodetachment timing. A removable (via a linear motion feed-through), dual micro-channel plate detector (MCP, Del Mar Ventures MCP-MA24/2) is located immediately after the VMI electrodes to provide mass spectral identification of cluster species for photodetachment.

The velocity map imaging electrodes were pulsed to high voltage 200 ns prior to the photodetachment event to ensure stable potentials. Photodetachment was performed via laser light produced by a dye laser (Lambda Physik LPD 3000) pumped by the second harmonic of a Nd:YAG laser (Quanta-Ray GCR-12S). The incident laser power was varied in order to keep the number of detected electrons at a rate of ~1 per laser pulse, but was typically on the order of a few microjoules at the point of entry into the chamber. To prevent deflection of the photodetached electrons by stray magnetic fields, the detection chamber was lined with magnetic shielding (Co-Netic 0.36 mm thickness, Magnetic Shield Corp.). The Co-Netic completely encapsulated the electron path, ensuring maximal shielding.

A position sensitive detector consisting of dual MCPs in a chevron configuration and a phosphor screen (Burle APD 2) was located 250 mm from the final electrode of the VMI assembly. A shielding cup was attached to the front of the MCP to prevent the deflection of electrons by the voltage applied to the rear of the MCP. To minimise background noise, the gain of the MCP was reduced such that no signal was observed and then pulsed up for a period of 50 ns at the arrival time of the signal electrons. Images were collected using a home built camera containing a charge-coupled device (CCD) sensor (Kodak, KAF-0402ME, 768 × 512 pixels). A lens (Navitar, 7000 TV Zoom) was fitted to the camera to allow for zooming and focusing of the image. Images were downloaded to a PC where the centres of each electron event were found and those events added to the growing two-dimensional, event-counted distribution. Due to the low signal rates, images at each photodetachment wavelength were collected over many hours and post-averaged.

A number of post-processing steps were applied to the raw experimental images before analysis. After collection, the ellipticity of the images was corrected. The circularisation method used in this study was designed by Lawrance and Gascooke[26] and has been used in previous VMI studies.[27,28] The process involves partitioning the image into wedges, each having a fixed angle and centred on the image centre. One wedge is taken as a reference wedge to which all other wedges can be compared. Radial features of each wedge are compared to the reference and the radial dimension is scaled linearly such that the features overlap. Au^- anion photodetachment was chosen as the primary calibrant in this study because of the strong signal, single photoelectron energy, and accurately determined electron affinity (EA).[18] Conversion of the final experimental image into a three-dimensional representation of the photodetachment event was achieved through the application of the inverse Abel transform.[29]

III. COMPUTATIONAL METHODS

The ground electronic states of the anion (singlet and triplet) and neutral (doublet) AuC_2 were calculated using both DFT and Coupled Cluster including single and double excitations and perturbative triples (CCSD(T)) methods. Initial structures were generated using the Kick algorithm developed by Addicoat and Metha[30] to generate random distributions of atoms and in some cases fragments within a specified subspace. In cases where the neutral equivalent of an anionic species did not converge, manually constructed geometries were employed. In addition, where "kicked" geometries possessed apparent point group symmetry, that symmetry was confirmed by re-optimization.

All initial DFT calculations were undertaken using the GAUSSIAN 09 suite of programs[31] employing the B3P86

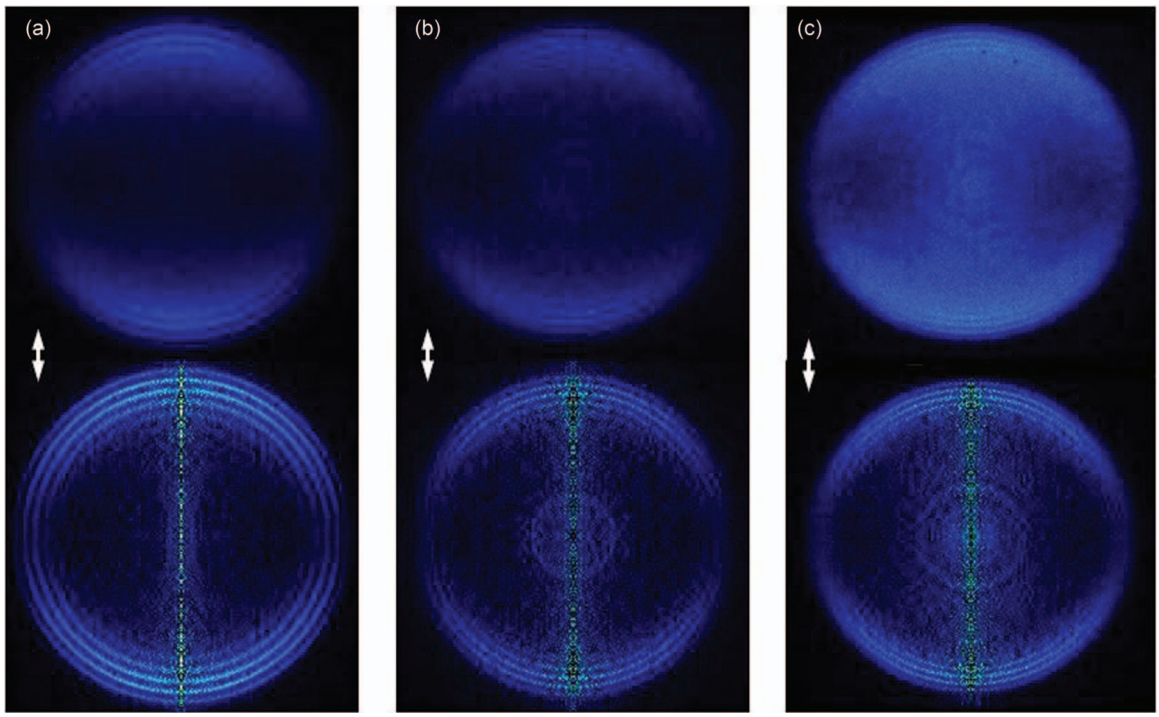

FIG. 1. Raw (upper) and processed (lower) images of AuC_2^- at photodetachment wavelengths of (a) 610 nm, (b) 585 nm, and (c) 560 nm, respectively. The arrow indicates the laser polarisation direction.

hybrid functional using the Stuttgart-Dresden (SDD) basis set. For Au, the MWB60 pseudopotential was used incorporating the first 60 electrons, leaving the remaining 19 to be calculated as valence. For carbon atoms, the Dunning/Huzinaga full double zeta (D95) basis set was used. The ground electronic states were re-optimized and frequency calculations were undertaken using CCSD(T), using the MOLPRO program.[32] In these calculations, carbon atoms were described using Dunning's aug-cc-pVDZ basis set[33] and the Au atom was described using aug-cc-pVDZ-PP and associated Effective Core Potential (ECP).[34,35] To verify the energies, further CCSD(T) single-point calculations were undertaken employing a higher quality aug-cc-pVQZ basis set for carbon atoms and the aug-cc-pVQZ-PP basis set. In order to consider spin-orbit effects, geometries of the anion and neutral were re-optimized within ADF,[36–38] employing first a scalar relativistic Hamiltonian and second the corresponding spin-orbit Hamiltonian.[39,40] These calculations employed the BP86 functional and all-electron TZ2P basis.[41] Since these additional calculations are completely consistent with the CCSD(T) calculations, they are not referred to further in the text but all calculated values are provided in Table S1 in the supplementary material.[57]

For all structures, harmonic frequency calculations were performed on the optimised geometries to confirm that they were true minima (i.e., no imaginary frequencies). The vibrational modes are labelled following the traditional nomenclature for linear triatomic molecules (i.e., ν_2 is the bending mode), and ν_1 and ν_3 are assigned as the C–C and Au–C stretching modes, respectively.

The relevant calculated structural and vibrational data were used as initial guess parameters for the simulation of Franck-Condon (FC) transition intensities for the prediction of the photodetachment spectra. FC simulations were performed with the ezSpectrum software suite[42] using the parallel approximation (i.e., FC factors are calculated as products of one-dimensional harmonic wavefunctions). Transitions emanating from the global minimum structure, as well as other isomers within 1 eV of the ground state, were calculated to compare against the experimental spectra. For each simulation, the energy of the 0_0^0 transition (1.442 eV), the applied convolution resolution (typically 15 meV), and the temperature (~200 K) were adjusted to obtain the best match to the experimental spectra.

IV. RESULTS

A. Velocity map images

The upper panels of Figs. 1(a)–1(c) show experimental velocity map images obtained from the photodetachment of AuC_2^- at laser wavelengths of 610 nm (2.04 eV), 585 nm (2.12 eV), and 560 nm (2.22 eV), respectively. The inverse Abel transformed images are presented in the lower panels of Figs. 1(a)–1(c).

A number of important observations can be immediately made from the experimental images. First, the well-resolved rings in the images suggest the excitation of a single vibrational progression of neutral AuC_2. Second, the image collected at 585 nm photodetachment also shows a sharp ring feature at a much reduced radius. This feature is also seen in the image taken at 560 nm but is not visible in the 610 nm image since the binding energy of the transition is greater than the photon energy. The third observation is that the intensity of the images at all three wavelengths is greater in the upper and lower portions of the rings, which is due to the anisotropy

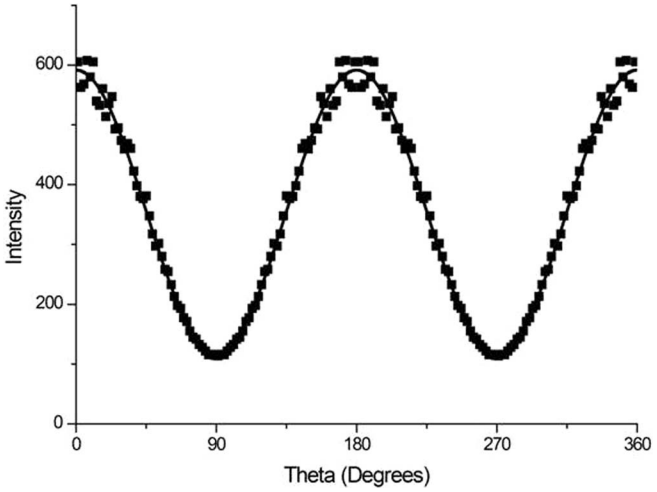

FIG. 2. Experimental angular intensity data from the image of AuC_2^- photodetachment at 610 nm (2.034 eV). The solid line fit represents the determination of β.

of the photodetachment process relative to the vertical polarisation direction of the laser. The degree of anisotropy is characterised by the angular dependent intensity, $F_\theta(\theta)$, defined by

$$F_\theta(\theta) = \frac{1}{4\pi}[1 + \beta P_2(\cos\theta)],$$

where $P_2(x)$ is the second order Legendre polynomial, $P_2(x) = \frac{1}{2}(3x^2 - 1)$, θ is the angle between the laser polarisation and angle of electron ejection, and β is the anisotropy parameter. β represents the degree of alignment between the direction of the photodetached electrons and the polarisation of the photodetachment laser and can take values between 2 and -1, the former corresponding to a $\cos^2\theta$ distribution and the latter to a $\sin^2\theta$ distribution. A β value of zero corresponds to an isotropic distribution.

Figure 2 shows the angular variation in intensity (data points) averaged over peaks 2–6 for the 610 nm excitation image, superimposed with the fit for β (solid line). The β values obtained for the three excitation wavelengths are 1.14 ± 0.03 (610 nm), 0.96 ± 0.12 (585 nm), 1.01 ± 0.04 (560 nm), where the uncertainties are 3σ as determined by the least-squares fitting algorithm. Wu *et al.*[17] have recently measured a value of 1.9 for the Au (^2S, $d^{10}s^1$) ← Au^- (^1S, $d^{10}s^2$) transition. This transition is ^2S ($d^{10}s^1$) ← ^1S ($d^{10}s^2$) and thus electrons are ejected in the form of a P wave, which corresponds to a β value of 2.[43] Based upon our spectral assignment (see below), the electron ejected from AuC_2^- is from the 19σ orbital, which we have described as having a significant Au 6*s*-orbital contribution. The positive β values measured here are consistent with this assignment.

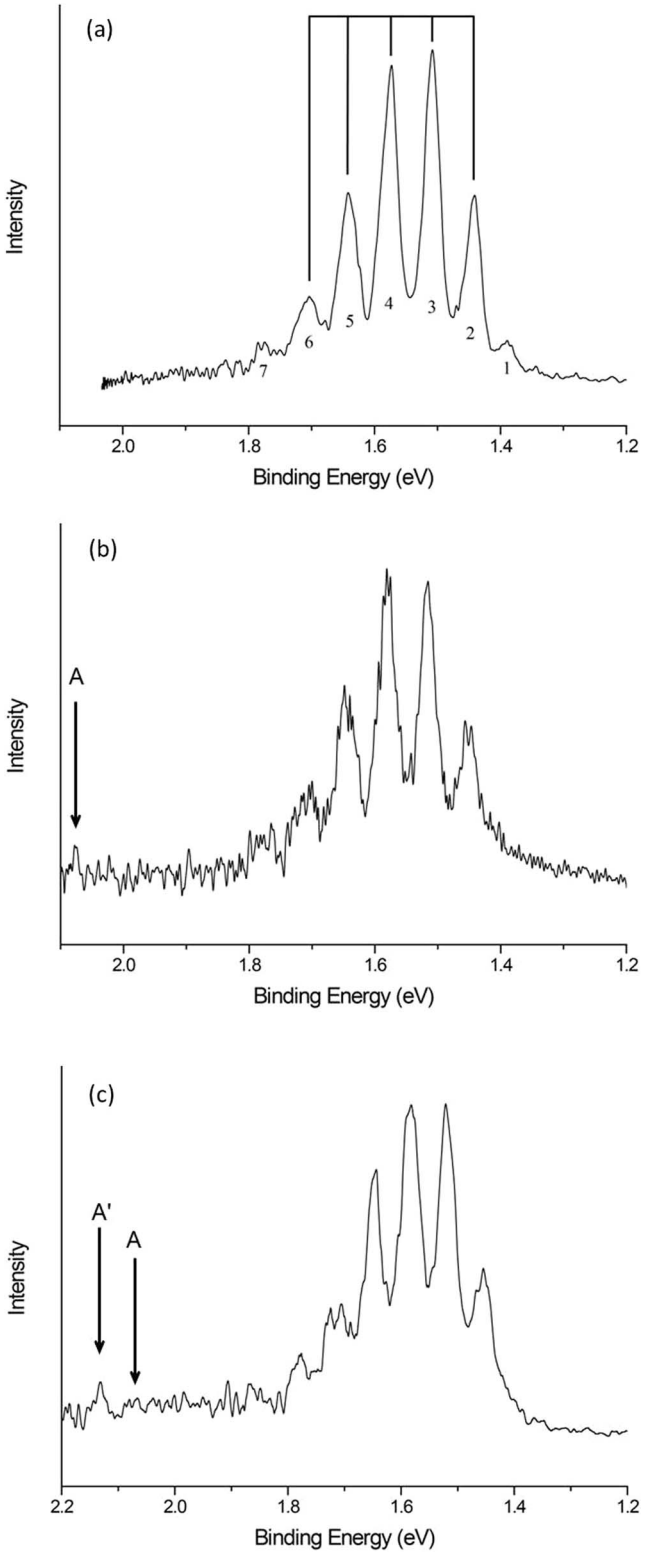

FIG. 3. Photodetachment binding energy spectrum of AuC_2^- collected at (a) 610 nm, (b) 585 nm, and (c) 585 nm excitation.

B. Binding energy spectra

Figures 3(a)–3(c) show the binding energy spectra obtained from Figs. 1(a) (610 nm), 1(b) (585 nm), and 1(c) (560 nm), respectively. For the spectrum collected at 610 nm, seven spectral features are identified, labelled 1–7, each with an observed full-width-half-maximum of ∼20 meV (160 cm^{-1}). A summary of the peak spacings extracted from the binding energy plot is shown in Table I. Peaks 2–6 are separated by a constant energy spacing of 528 ± 5 cm^{-1} and are assigned to a single vibrational progression, X_0^n, in the upper state (i.e., neutral AuC_2). Peak 7 also seems to belong to this progression but shows an increased spacing of 543 cm^{-1}

TABLE I. Peak positions, peak separations, and assignments taken from the binding energy spectrum collected at a photodetachment wavelength of 610 nm.

Peak	Binding energy (eV)	Separation (cm^{-1})	Assignment
1	1.388	...	3_1^0
2	1.442	436	0_0^0
3	1.507	524	3_0^1
4	1.573	532	3_0^2
5	1.638	524	3_0^3
6	1.704	532	3_0^4
7	1.771	540	3_0^5

(from peak 6), which may be explained by the relatively poor signal-to-noise ratio masking the true peak position. The energy spacing between peaks 1 and 2 is significantly reduced versus the primary progression (436 versus 528 cm^{-1}). Given that the position of peak 1 is at the red end of the spectrum, it is proposed that this feature represents a hot band transition, X_1^0. Thus, the spacing between peaks 1 and 2 provides the vibrational frequency of the vibrational mode in anionic AuC_2. From this assignment, peak 2 at 1.442 eV is assigned to the origin transition, 0_0^0.

The binding energy spectra collected at a photodetachment wavelengths of 585 and 560 nm match the corresponding spectrum recorded using 610 nm, albeit at a slightly reduced resolution that is associated with the higher electron kinetic energies. The feature defined as the hot band (i.e., peak 1) is not visible and the energy spacing between each of the remaining peaks is less well determined due to the reduced signal-to-noise ratio. The average spacing of peaks 2–5 was observed to be 521 ± 5 cm^{-1}, which agrees with the value of 528 ± 5 cm^{-1} obtained from the 610 nm spectrum. The additional feature of the image collected at 585 nm mentioned earlier in the article is marked on the plot as feature **A**. Although it has a low relative intensity, feature **A** is very well defined and lies at a binding energy of 2.078 eV, which lies 0.616 eV or 4970 cm^{-1} above the assigned 0_0^0 transition. Given this significant energy difference of feature **A**, we associate this peak to a different electronic transition. Further analysis of this feature is provided later in light of the computational results.

C. Calculations

Several types of geometric structures for AuC_2 are possible, including (i) linear or bent Au–C_α–C_β, (ii) T-shaped (i.e., side-on), (iii) linear or bent C–Au–C. These possibilities have been theoretically and experimentally investigated for

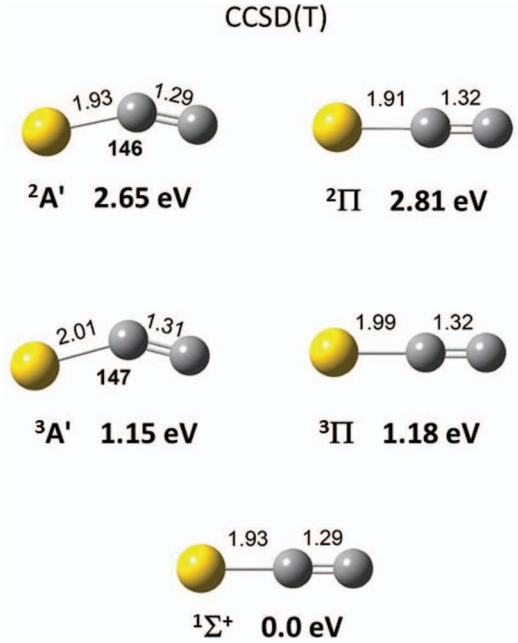

FIG. 4. Lowest anion and neutral geometries obtained for the CCSD(T) calculations. Electronic energies are given relative to the global minimum neutral structure. The units for bond length are Angstroms and degrees for bond angle.

the neutral and cationic 3*d* M–C_2 molecules.[44,45] For CuC_2, the preferred arrangement was found to be T-shaped, however, the iso-electronic species ZnC_2, which is iso-valent with AuC_2^-, was shown to prefer a linear arrangement (i.e., ZnCC) at the multi-reference configuration interaction level (MRCI) of theory. We find in all of our calculations for AuC_2^- that only structures involving bonding of type (i) are energetically competitive. All other arrangements were found to be transition states or much higher in energy.

Both DFT and CCSD(T) calculations find the global minimum of AuC_2^- to be a linear $^1\Sigma^+$ state; geometries for the latter are shown in Figure 4 (the DFT results are not shown but are very similar). Results of harmonic frequency calculations for each minimum are also presented in Table II. Analysis of the molecular orbitals (MOs) involved, including a calculation with an $Au^{\delta-}$–$C_2^{\delta-}$ separation of 10 Å, reveals a molecular orbital diagram shown in Figure 5. This MO picture is similar to that previously presented for AuO^-, which also has a $^1\Sigma^+$ ground state.[46] This is unsurprising given that the electronic structure of C_2 is iso-valent with the O atom, having 4 electrons in a π-type orbital and an unoccupied σ-type (of course these orbitals are degenerate in the O atom and the occupation is either $\sigma^1\pi^3$ or $\sigma^2\pi^2$). The largest difference

TABLE II. Relative energies (eV) harmonic vibrational frequencies (cm^{-1}), and Mulliken population charges (e) for the $^1\Sigma^+$, ^{3}**A′**, $^3\Pi$, ^{2}**A′**, and $^2\Pi$ states calculated at CCSD(T)/aug-cc-pVDZ (see details in text).

State	ΔE	ω_1 C–C stretch	ω_2 Au–C–C bend	ω_3 Au–C stretch	q(Au)	q(C_α)	q(C_β)
$^2\Pi$	2.81	1743	193	480	0.35	−0.29	−0.06
^{2}**A′**	2.65	1541	204	534	0.35	−0.30	−0.05
$^3\Pi$	1.18	1732	184	398	− 0.53	−0.23	−0.24
^{3}**A′**	1.15	1659	122	427	− 0.50	−0.28	−0.22
$^1\Sigma^+$	0.00	1830	190	457	− 0.20	−0.47	−0.33

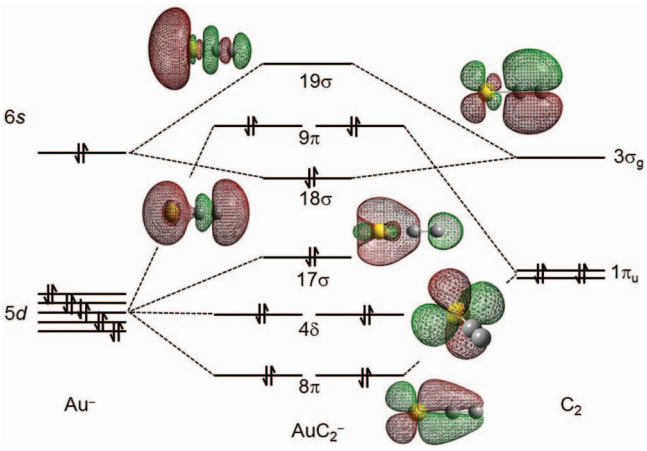

FIG. 5. Schematic representation of molecular orbitals and electronic configuration of the $^1\Sigma^+$ state of AuC_2^-.

between AuC_2^- and AuO^- is the relative ordering of the bonding orbitals involving the Au 5*d* orbitals.

The MOs in Figure 5 represent the end-on interaction of the ^1S state of Au^- with the $^1\Sigma^+$ state of C_2. The frontier orbitals are 18σ, 9π, and 19σ; the latter being the unoccupied LUMO for the 92 electron anion. The 19σ orbital is the anti-bonding combination of the (unfilled) C_2 σ-orbital and Au 6*s*-orbital mixed with $5d\sigma$ character, the 9π orbital is the anti-bonding combination of the C_2 π-orbital and Au $5d\pi$-orbital, and the 18σ orbital is the Au–C bonding combination of the C_2 σ-orbital and Au 6*s* orbital. Occupation of the 18σ orbital indicates charge transfer from the 6*s* orbital into the C_2 σ-orbital, which is supported by the Mulliken population analysis (see Table II) that shows the Au atom is slightly negatively charged at -0.20 *e*, with C_α and C_β sharing most of the charge at -0.47 and -0.33 *e*, respectively.

The CCSD(T) calculations predict a relatively low-lying bent triplet state, $^3\mathbf{A'}$ state, 1.15 eV above the singlet global energy minimum (see Table II). The bond angle is 147°, as shown in Figure 4. From inspection of the molecular orbitals, this state has configuration $(9\pi)^4(18\sigma)^1(19\sigma)^1$, which would give rise to a $^3\Sigma^+$ state in $C_{\infty v}$. The MO configuration predicts that electron transfer into the 19σ anti-bonding orbital would lead to an increase in the Au–C_α bond length relative to the $^1\Sigma^+$ state, as shown in Figure 4 (2.01 cf. 1.93 Å). The Mulliken populations in Table II indicate a transfer of electron density onto Au atom (-0.50 *e*) at the expense of both C_α (-0.28 *e*) and C_β (-0.22 *e*). At the linear geometry ($^3\Sigma^+$ state), we have calculated that the energy increases by only 0.025 eV ($\sim$205 cm^{-1}). This barrier to linearity lies just above the zero-point energy of the bending mode (see Table II), suggesting that the molecule could be considered pseudo-linear in this state.

We also identify a second triplet state, but linear, only 0.03 eV higher than the $^3\mathbf{A'}$ state. This state arises from the configuration $(18\sigma)^2(9\pi)^3(19\sigma)^1$, which would give rise to a $^3\Pi_i$ state. Such a state has been calculated for AuO^- to lie only 0.23 eV above the ground $^1\Sigma^+$ state.[47] Again, population of the 19σ anti-bonding orbital should lead to an increase in the Au–C_α bond length, just as calculated (i.e., 1.99 Å). The Mulliken populations for this state show that the atomic charges are similar to the $^3\mathbf{A'}$ state (Table II). This $^3\Pi_i$ state can also exhibit spin-orbit (SO) splitting, which is expected to be large for an Au-containing molecule. The ^2D $(5d)^9(6s)^2$ state of Au has SO components at 9161 cm^{-1} ($J = 5/2$) and 21 435 cm^{-1} ($J = 3/2$), yielding $\zeta_{5d}(\mathrm{Au}) = -4909.6$ cm^{-1} (0.6 eV).[48] Lefebvre-Brion and Field[49] describe that for a $^3\Pi$ state the $E^{SO} = \mathbf{A}\Lambda\Sigma$ where $\mathbf{A} = -|c_{5d\pi\,\mathrm{Au}}|^2\zeta_{5d}(\mathrm{Au})/2$. For AuC_2^-, the SO splitting depends upon the degree of Au 5*d* character in the unpaired 9π orbital, which our calculations suggest will be $\sim$20% Therefore, the $^3\Pi_i$ sub-states are expected to be separated by $\mathbf{A} \sim 500$ cm^{-1}.

For neutral AuC_2, we find a bent $^2\mathbf{A'}$ state, 2.65 eV, above the singlet global energy minimum (see Table II). The structure has a $\angle_{\mathrm{Au\text{–}C\text{–}C}}$ bond angle of 146°, and Au–C and C–C bond lengths of 1.93 Å and 1.29 Å, as shown in Figure 4. This state has configuration $(18\sigma)^1(9\pi)^4$ and results from the loss of an electron from the 18σ orbital leading to the bent geometry. For AuO, this configuration has been calculated to result in a $^2\Sigma^+$ state lying 1.34 eV (10 808 cm^{-1}) above the ground $^2\Pi$ state.[50] Our Mulliken population for the $^2\mathbf{A'}$ shows that the Au–C_α bond is ionic, with equal but opposite charges on Au ($+0.35$ *e*) and C_α, (-0.3 *e*), and the C_β atom becoming neutral (Table II). The linear ($^2\Sigma^+$) form of this state is calculated to be 0.06 eV ($\sim$500 cm^{-1}) above the bent geometry. In this case, the calculated barrier height comfortably exceeds the zero-point energy of the bend (see Table II), indicating that this electronic state is probably not pseudo-linear like the $^3\mathbf{A'}$ state.

We also identify a linear $^2\Pi_i$ state arising from a $(18\sigma)^2(9\pi)^3$ configuration only 0.16 eV higher in energy than the $^2\mathbf{A'}$ state, and with a similar Mulliken population. As discussed above, this state can exhibit SO splitting due to the unpaired 9π orbital. For a $^2\Pi$ state, Lefebvre-Brion and Field[49] show that $\mathbf{A} = -|c_{5d\pi\,\mathrm{Au}}|^2\zeta_{5d}(\mathrm{Au})$, which puts the $^2\Pi_{3/2}$ and $^2\Pi_{1/2}$ sub-states at $+500$ and -500 cm^{-1}, respectively (again assuming 20% Au 5*d* character in the orbital). This is similar to that observed in the analogous $^2\Pi$ state of AuO, where the SO splitting has been directly observed to be -1440 ± 80 cm^{-1}, and predicted to be $\sim$1000 cm^{-1} based upon a calculation that the π MO has $\sim$20% atomic Au 5*d* character.[46,51]

Cohen *et al.*[15] have previously reported DFT calculated structures for neutral and cationic AuC_2. Using the B3LYP/LANL2DZ combination, they calculated the AuC_2 neutral to be bent (angle unspecified) with doublet multiplicity, which seems to be consistent with our DFT and CCSD(T) results. They also found a doublet C_{2v} structure to be only 0.26 eV higher in energy. They calculated the cation to have a bent ($\angle_{\mathrm{Au\text{–}C\text{–}C}} = 160°$) structure with triplet multiplicity; a bent singlet was found 1.06 eV higher in energy. Using the more computationally expensive MPW1PW91/SDD combination, they found the lowest energy cation to be a linear triplet state, however, these workers did not report an optimised structure for neutral AuC_2 at this level of theory.

All of the electronic states we have considered for anionic and neutral AuC_2 are summarised in Figure 6, which separates the states by energy (vertical axis) and Au–C bond length (horizontal axis). The electronically allowed transitions that can occur for AuC_2^- are represented with arrows

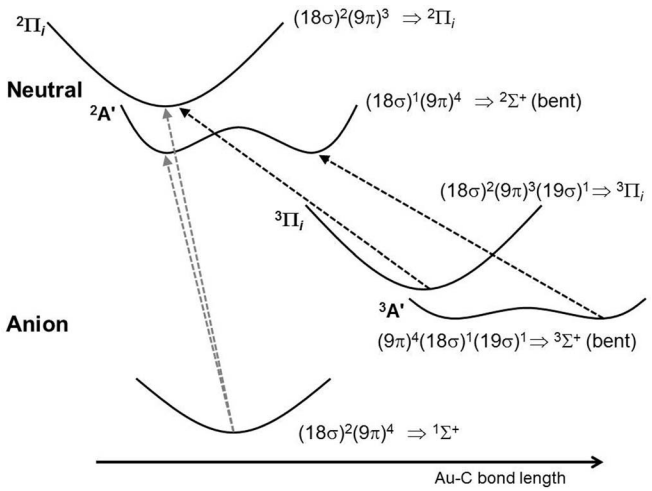

FIG. 6. Schematic diagram of the energy levels of anionic and neutral AuC_2, and possible photodetachment transitions. The coordinate along the x-direction reflects the Au–C bond length and the potential curves represent the Au–C–C bond angle.

in Figure 6. Two transitions involving photodetachment from the lowest anion state; $^2\mathbf{A'} \leftarrow {}^1\Sigma^+$ and $^2\Pi \leftarrow {}^1\Sigma^+$ are calculated to occur at 2.65 and 2.81 eV. For each of the triplet states, only one one-electron transition is permitted; $^2\mathbf{A'} \leftarrow {}^3\mathbf{A'}$ and $^2\Pi \leftarrow {}^3\Pi$ are calculated to occur at 1.50 and 1.63 eV, respectively. In Sec. V, we consider each transition using Franck-Condon simulations to identify the observed spectrum at 1.442 eV and also the higher energy feature at 2.078 eV.

V. DISCUSSION

A. Vibronic structure of the 1.442 eV transition

As mentioned above, the relatively simple vibrational structure seen in Figure 3 (with energy spacings reported in Table I) suggests that only a single vibrational mode dominates the spectrum. The observed spacing of 528 cm^{-1} best corresponds to the calculated value for ν_3 in the neutral molecule in both the $^2\mathbf{A'}$ and $^2\Pi$ states (534 cm^{-1} and 480 cm^{-1}, respectively – see Table II) i.e., the progression is 3_0^n. The hot band transition, located 436 cm^{-1} from the origin, also closely matches all values calculated for ν_3 in the triplet and singlet states of the anion.

Further information can be obtained by considering the overall band structure and comparing it with calculated Franck-Condon factors which take into account initial and final geometries, as well as calculated vibrational frequencies. We have simulated a number of transitions based on the CCSD(T) calculated structures. For all simulations, the origin band is fixed to appear at 1.442 eV and the vibronic temperature is assumed to be 200 K, as discussed below.

We first consider the transition arising from the calculated AuC_2^- global minimum, the linear singlet state $^1\Sigma^+$, to the AuC_2 neutral bent ground electronic state $^2\mathbf{A'}$ and the linear $^2\Pi$ state. For the $^2\mathbf{A'} \leftarrow {}^1\Sigma^+$ transition, the molecule undergoes a significant bond angle reduction of 34° but almost no change in the Au–C_α and C_α–C_β bond lengths. The simulated spectrum is thus expected to involve significant activity in the bend. As expected, the simulated spectrum, shown in Figure 7(a), displays significant excitation of the low frequency bending vibration (ν_2). Clearly, it does not come close to matching the experimental spectra in Figure 3. The $^2\Pi \leftarrow {}^1\Sigma^+$ transition involves a 2 pm reduction in the Au–C_α bond and a 3 pm extension of the C_α–C_β bond. The simulated spectrum in Figure 7(c) shows a short progression in the C–C stretch and no activity in the bending mode, as expected. Again, it bears no resemblance to the experimental spectrum.

We next consider the transition from the next lowest electronic state of the anion, the $^3\mathbf{A'}$ state, to the ground $^2\mathbf{A'}$ state of the neutral. This is a bent state, although it is unclear whether the zero-point energy lies above or below the barrier. The calculated geometry change involves an 8 pm decrease in the Au–C_α bond length and virtually no change in bond angle, and so we expect a progression in the Au–C stretch mode. The resultant simulation in Figure 7(b) shows excitation of the Au–C stretch (ν_3), which closely resembles the experimental spectrum, with the only slight discrepancy being that the 0_0^0 transition is calculated to be slightly too intense (i.e., it is not the most intense peak in the experimental spectrum). Furthermore, the calculated vibrational frequency for the neutral $^2\mathbf{A'}$ state (534 cm^{-1}) closely matches the observed spacing of 528 cm^{-1}. The ν_3 frequency of the anion $^3\mathbf{A'}$ state (427 cm^{-1}) is also close to the observed hot band value of 436 cm^{-1}, although we note that this level is calculated to lie above the barrier to linearity. Underlying each of the main progression peaks is a small shoulder, which is due to activity of ν_2 arising from the very slight (1°) bond angle change. This feature seems to be present in the experimental spectrum, where each vibronic peak has a slight asymmetric broadening at higher binding energy, consistent with the simulation. From the simulation, one can estimate the vibrational temperature of the molecular beam (i.e., Boltzmann distribution). Varying the initial temperature of the FC simulations causes the intensity of the hot band (located at just under 1.4 eV) to vary due to the changed population in the low lying vibrational levels of the anion. The temperature found to produce the best match to experiment involved a vibrational temperature of 200 ± 50 K, which is the value used for Figs. 7(a)–7(d).

The transition from the linear triplet state, i.e., $^2\Pi \leftarrow {}^3\Pi$, involves an 8 pm reduction in the Au–C bond length and no change in the C–C bond length nor (obviously) in the bond angle; the FC simulated spectrum is presented in Figure 7(d). The predicted spectrum shows a strong progression in ν_3, and is a reasonable comparison to the experimental spectrum. However, the calculated ν_3 frequency for the $^2\Pi$ state, 480 cm^{-1}, is a bit too low (cf. 528 cm^{-1}), the progression length is slightly shorter than in 7(b) due to the slightly smaller change in Au–C bond length calculated for this transition, and each peak is narrow and symmetric since there is no bending mode activity to broaden the vibronic transition. Finally, there are expected spin-orbit bands associated with the $^2\Pi \leftarrow {}^3\Pi$ transition that are not included in the simulations. For electron detachment, we expect the following sub-bands to be electronically allowed; $^2\Pi_{3/2} \leftarrow {}^3\Pi_2$,

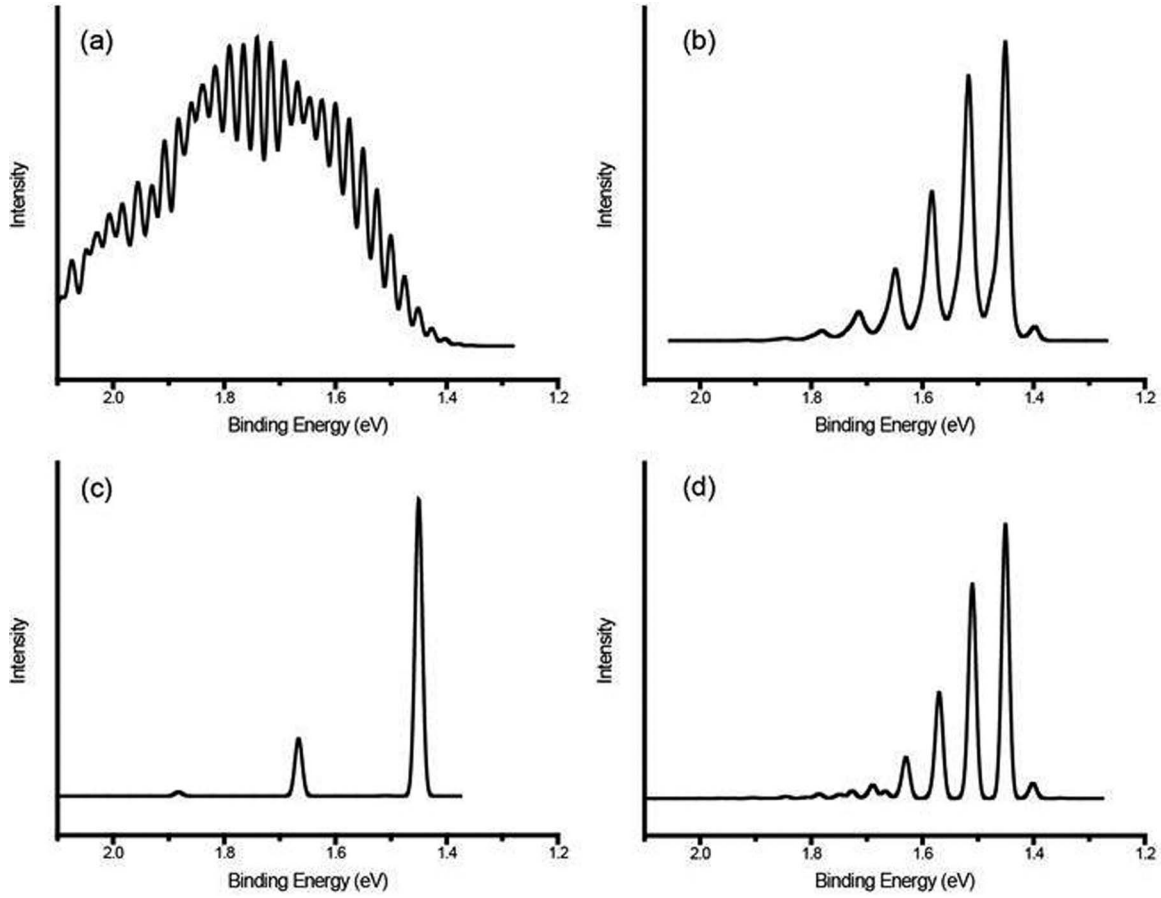

FIG. 7. Franck-Condon spectral simulations of the binding energy spectra using the calculated CCSD(T) parameters; (a) $^2\mathbf{A'} \leftarrow {}^1\Sigma^+$, (b) $^2\mathbf{A'} \leftarrow {}^3\mathbf{A'}$, (c) $^2\Pi \leftarrow {}^1\Sigma^+$, and (d) $^2\Pi \leftarrow {}^3\Pi$ transitions.

$^2\Pi_{3/2} \leftarrow {}^3\Pi_1$, $^2\Pi_{1/2} \leftarrow {}^3\Pi_1$, $^2\Pi_{1/2} \leftarrow {}^3\Pi_0$. Therefore, if this transition is responsible for the spectrum observed three bands are expected, ~500 cm^{-1} apart, and this is not evident in the experimental spectrum (assuming spin-orbit quenching does not occur).

Both the simulated $^2\mathbf{A'} \leftarrow {}^3\mathbf{A'}$ and $^2\Pi_{3/2} \leftarrow {}^3\Pi_2$ transitions provide good comparison with the experimental spectrum. The predicted energies for the two transitions are 1.50 and 1.63 eV, respectively, both of which agree with the observed origin at 1.442 eV. However, due to the better match of the $^2\mathbf{A'} \leftarrow {}^3\mathbf{A'}$ transition in terms of frequency, progression length, and peak width, as well as the lack of any obvious spin-orbit features in the observed spectrum, we prefer the assignment of this transition to the experiment. The assignment of the prominent spectrum to originate from an electronic state calculated to lie over 1 eV above the global energy minimum may seem unusual. However, the ability of meta-stable electronic states to trap significant population due to inefficient, forbidden spin-crossing between triplet and singlet states, even at relatively large energy gaps, is well documented for metal clusters, including our own previous work on niobium-carbide clusters (and references therein).[52]

Finally, it is also worth commenting on the similarity of the observed spectrum with the PES spectrum recorded for $AuOH^-$ by Bowen and co-workers.[53] The observed spectral envelope of AuOH, involving six quanta of the Au–O stretch (ν_3), is attributed to a shortening of the Au–O bond by 12 pm, similar to that predicted for AuC_2. This similarity supports our proposal that the observed vibronic structure arises from excitation out of a bent $^3\mathbf{A'}$ state that is not the global minimum.

B. Feature A at 2.078 eV

We now turn our attention to feature **A**, which lies 0.616 eV (4970 cm^{-1}) above the assigned 0_0^0 transition. While weak in Figure 3(b), it is clearly evident in the raw image shown in Figure 1(b) (i.e., 585 nm excitation). The feature must be associated with another electronic transition, since it does not form part of the lower energy progression.

At the photodetachment wavelength of 560 nm (2.22 eV), the binding energy spectrum (Figure 3(c)) continues for 0.12 eV (~970 cm^{-1}) beyond where feature **A** appears. An analysis of this image reveals that feature **A** is now very weak (appearing just above the noise) and that a stronger feature, labelled **A′**, appears approximately 460 ± 20 cm^{-1} higher in energy. The signal-to-noise level in the inverse Abel transformed image is poor in this region due to the significant contribution to the raw image from the more intense $^2\mathbf{A'} \leftarrow {}^3\mathbf{A'}$ transition, however, these features are more clearly seen in the processed velocity map image of Figure 1(c).

Given that the calculations predict the global energy minimum to be associated with the linear $^1\Sigma^+$ state some ~1.1 eV lower than the bent triplet state, it is tempting to assign feature **A** to a transition arising from this state. However, the spectral predictions for the $^2\mathbf{A}' \leftarrow {}^1\Sigma^+$ and $^2\Pi \leftarrow {}^1\Sigma^+$ (Figs. 7(a) and 7(c), respectively) do not fit the observed, albeit weak, features that involve a vibrational spacing of ~460 cm^{-1}. Furthermore, the calculated transition energies, at 2.65 eV and 2.81 eV, respectively, are slightly too large.

An alternative, and our preferred, assignment for feature **A** is that it is due to the $^2\Pi \leftarrow {}^3\Pi$ transition. The observed spacing of 460 cm^{-1} matches the calculated value of ν_3 for the $^2\Pi$ state and the spectral simulation for this transition. The spectral intensity is expected to be weaker due to the reduced thermal population of the $^3\Pi$ state relative to $^3\mathbf{A}'$, and also because its intensity is diluted over several spin-orbit sub-bands. The calculated transition energy, ~0.2 eV higher than the $^2\mathbf{A}' \leftarrow {}^3\mathbf{A}'$ transition, does not match the observed energy difference but the spin-orbit effects may be quite different from the first-order treatment presented above.

Clearly, further experimental work is required on this system at shorter photodetachment wavelengths, which we are preparing to do. It would also be useful to "cool" population out of the excited triplet state(s) to the $^1\Sigma^+$ global minimum, thereby increasing the intensity of transitions from this state and decreasing the contribution to the images from the $^2\mathbf{A}' \leftarrow {}^3\mathbf{A}'$ transition.

C. Comparison with other metal-dicarbide species

Wang and co-workers have investigated the series of 3*d* transition metal-dicarbides using PES; ScC_2,[9] TiC_2,[10] VC_2,[9,13] CrC_2,[9,13] MnC_2,[9] FeC_2,[9,12,13] and CoC_2.[9,13] For all molecules, both in the ground anionic and excited neutral states, they found the spectra to be consistent with molecules where the metal atom is side-bonded onto the C_2 group with C_{2v} symmetry (i.e., "T-shaped"). The trends of measured EAs and vibrational frequencies for the series were found to correlate well with the corresponding monoxides, suggesting that the chemical bonding in MC_2 is analogous to that in M–O (i.e., ionic) and that MC_2 may be qualitatively considered as $M^{2+}C_2^{2-}$. These workers also investigated the 4*d* molecule NbC_2[11] and found the structure and bonding to be the same as for the 3*d* metal-dicarbides.

The electronic spectrum of neutral YC_2 has been observed by Steimle and co-workers[54–56] using laser induced fluorescence and optical Stark spectroscopy. Their high resolution analysis showed that the ground state molecule is T-shaped with C_{2v} symmetry and is highly ionic.

Clearly, the structure of AuC_2 that we deduce from our study is quite different from that of the other known transition metal-dicarbide molecules. Based upon this, it may be expected that the iso-valent CuC_2 and AgC_2 molecules will have similar bent, or quasi-linear, structures. However, there are no experimental spectroscopic evidence for their structures. Using DFT and QCISD, Largo and co-workers[44] have calculated the CuC_2 neutral molecule to be T-shaped, however, a linear CuCC arrangement was found to be lower in energy for the cation.[45] To our knowledge, there are no calculations on the structure of AgC_2. Clearly, determining the structure of these iso-valent species would provide an interesting comparison with the AuC_2 case.

VI. CONCLUSIONS

In summary, the $AuC_2 \leftarrow AuC_2^-$ transition was investigated using velocity map imaging of photoelectrons. The EA, vibrational frequencies, and geometry changes obtained from the binding energy spectra are reported for the first time. Density functional theory and coupled cluster calculations were performed in order to determine the ground state structures of the anion and neutral species and assist in the assignment of the experimental spectra. It was found that the lowest lying anion structure, a linear singlet, was not the initial state for the observed vibronic structure as the Franck-Condon simulated spectra involving this species were a poor match to the experimental data. The best assignment for this experimental transition was found to be from an excited triplet state $^2\mathbf{A}' \leftarrow {}^3\mathbf{A}'$, calculated to be approximately 1.2 eV higher in energy than the linear ground state. The observed spectrum is consistent with the AuC_2 anion having a bent structure that is excited to a neutral state that has a small, or no, change in $\angle_{Au-C-C}$ bond angle and a ~8 pm change in the Au–C bond length.

ACKNOWLEDGMENTS

Financial support from Flinders University and the University of Adelaide is gratefully acknowledged. Support from the Australian Research Council for the purchase and maintenance of the lasers is also acknowledged. Computing resources provided by the National Computational Infrastructure (NCI) Facility and eResearch SA is also gratefully acknowledged.

[1] D. S. Bethune, C. H. Kiang, M. S. De Vries, G. Gorman, R. Savoy, J. Vazquez, and R. Beyers, Nature (London) **363**, 605 (1993).
[2] D. E. Clemmer, K. B. Shelimov, and M. F. Jarrold, Nature (London) **367**, 718 (1994).
[3] S. Roszak and K. Balasubramanian, J. Chem. Phys. **106**, 158 (1997).
[4] D. L. Strout and M. B. Hall, J. Phys. Chem. A **102**, 641 (1998).
[5] B. C. Guo, K. P. Kerns, and A. W. Castleman, Jr., Science **255**, 1411 (1992).
[6] B. C. Guo, S. Wei, J. Purnell, S. Buzza, and A. W. Castleman, Jr., Science **256**, 515 (1992).
[7] M. A. Duncan, J. Cluster Sci. **8**, 239 (1997).
[8] P. Liu, J. M. Lightstone, M. J. Patterson, J. A. Rodriguez, J. T. Muckerman, and M. G. White, J. Phys. Chem. B **110**, 7449 (2006).
[9] X. Li and L.-S. Wang, J. Chem. Phys. **111**, 8389 (1999).
[10] X.-B. Wang, C.-F. Ding, and L.-S. Wang, J. Phys. Chem. A **101**, 7699 (1997).
[11] H.-J. Zhai, S.-R. Liu, X. Li, and L.-S. Wang, J. Chem. Phys. **115**, 5170 (2001).
[12] J. Fan and L. S. Wang, J. Phys. Chem. **98**, 11814 (1994).
[13] Y.-B. Yuan, K.-M. Deng, Y.-Z. Liu, and C.-M. Tang, Chin. Phys. Lett. **23**, 1761 (2006).
[14] H.-J. Zhai, L.-S. Wang, P. Jena, G. L. Gutsev, and C. W. Bauschlicher, Jr., Chem. Phys. **120**, 8996 (2004).
[15] Y. Cohen, V. Bernshtein, E. Armon, A. Bekkerman, and E. Kolodney, J. Chem. Phys. **134**, 124701 (2011).
[16] A. T. J. P. Eppink and D. H. Parker, Rev. Sci. Instrum. **68**, 3477 (1997).
[17] X. Wu, Z. Qin, H. Xie, R. Cong, X. Wu, Z. Tang, and H. Fan, J. Chem. Phys. **133**, 044303 (2010).

[18]J. Ho, K. M. Ervin, and W. C. Lineberger, J. Chem. Phys. **93**, 6987 (1990).
[19]H.-J. Zhai, B. Kiran, and L.-S. Wang, J. Chem. Phys. **121**, 8231 (2004).
[20]X. Wang and L. Andrews, J. Am. Chem. Soc. **123**, 12899 (2001).
[21]L. Andrews and X. Wang, J. Am. Chem. Soc. **125**, 11751 (2003).
[22]Y.-L. Wang, X.-B. Wang, X. Xing, F. Wei, J. Li, and L.-S. Wang, J. Phys. Chem. A **114**, 11244 (2010).
[23]B. W. Ticknor, B. Bandyopadhyay, and M. A. Duncan, J. Phys. Chem. A **112**, 12355 (2008).
[24]M. W. Heaven, G. M. Stewart, M. A. Buntine, and G. F. Metha, J. Phys. Chem. A **104**, 3308 (2000).
[25]J. H. D. Eland, Meas. Sci. Technol. **4**, 1522 (1993).
[26]J. R. Gascooke, Ph.D. dissertation, Flinders University of South Australia, 2000.
[27]S. J. Cavanagh, S. T. Gibson, M. N. Gale, C. J. Dedman, E. H. Roberts, and B. R. Lewis, Phys. Rev. A **76**, 052708 (2007).
[28]M. van Duzor, F. Mbaiwa, J. Wei, T. Singh, R. Mabbs, A. Sanov, S. J. Cavanagh, S. T. Gibson, B. R. Lewis, and J. R. Gascooke, J. Chem. Phys. **133**, 174311 (2010).
[29]E. W. Hansen and P.-L. Law, J. Opt. Soc. Am. A **2**, 510 (1985).
[30]M. A. Addicoat and G. F. Metha, J. Comput. Chem. **30**, 57 (2009).
[31]M. J. Frisch, G. W. Trucks, H. B. Schlegel *et al.*, GAUSSIAN 09, Revision B.01, Gaussian Inc., Wallingford, CT, 2009.
[32]H.-J. Werner, P. J. Knowles, G. Knizia, F. R. Manby, M. Schütz *et al.*, MOLPRO, version 2010.1, a package of *ab initio* programs, see http://www.molpro.net.
[33]R. A. Kendall, T. H. Dunning, Jr., and R. J. Harrison, J. Chem. Phys. **96**, 6796 (1992).
[34]K. A. Peterson and C. Puzzarini, Theor. Chem. Acc. **114**, 283 (2005).
[35]D. Figgen, G. Rauhut, M. Dolg, and H. Stoll, Chem. Phys. **311**, 227 (2005).
[36]G. te Velde, F. M. Bickelhaupt, S. J. A. van Gisbergen, C. F. Guerra, E. J. Baerends, J. G. Snijders, and T. Ziegler, J. Comput. Chem. **22**, 931 (2001).
[37]C. F. Guerra, J. G. Snijders, G. te Velde, and E. J. Baerends, Theor. Chem. Acc. **99**, 391 (1998).
[38]ADF2012, SCM, Theoretical Chemistry, Vrije Universiteit, Amsterdam, The Netherlands, 2012, see http://www.scm.com.
[39]E. van Lenthe, E. J. Baerends, and J. G. Snijders, J. Chem. Phys. **101**, 9783 (1994).
[40]E. van Lenthe, A. E. Ehlers, and E. J. Baerends, J. Chem. Phys. **110**, 8943 (1999).
[41]E. van Lenthe and E. J. Baerends, J. Comput. Chem. **24**, 1142 (2003).
[42]V. A. Mozhayskiy and A. I. Krylov, ezSpectrum 3.0, see http://iopenshell.usc.edu/downloads.
[43]N. D. Gibson, B. J. Davies, and D. J. Larson, Phys. Rev. A **48**, 310 (1993).
[44]V. M. Rayón, P. Redondo, C. Barrientos, and A. Largo, Chem. Eur. **12**, 6963 (2006).
[45]V. M. Rayón, P. Redondo, C. Barrientos, and A. Largo, J. Phys. Chem. A **111**, 6345 (2007).
[46]T. Ichino, A. J. Gianola, D. H. Andrews, and W. C. Lineberger, J. Phys. Chem. A **108**, 11307 (2004).
[47]M. L. Kimble, A. W. Castleman, Jr., R. Mitrić, C. Bürgel, and V. Bonačić-Koutecký, J. Am. Chem. Soc. **126**, 2526 (2004).
[48]A. Kramida, Y. Ralchenko, J. Reader, and NIST ASD Team, NIST Atomic Spectra Database (version 4.1.1), National Institute of Standards and Technology, Gaithersburg, MD, 2012, see http://physics.nist.gov/asd.
[49]H. Lefebvre-Brion and R. W. Field, *The Spectra and Dynamics of Diatomic Molecules* (Academic Press, Amsterdam, 2004).
[50]P. Schwerdtfeger, M. Dolg, W. H. E. Schwarz, G. A. Bowmaker, and P. D. W. Boyd, J. Chem. Phys. **91**, 1762 (1989).
[51]L. C. O'Brien, S. C. Hardimon, and J. J. O'Brien, J. Phys. Chem. A **108**, 11302 (2004).
[52]V. Dryza, M. A. Addicoat, J. R. Gascooke, M. A. Buntine, and G. F. Metha, J. Phys. Chem. A **112**, 5582 (2008).
[53]W. Zheng, X. Li, S. Eustis, A. Grubisic, O. Thomas, H. de Clercq, and K. Bowen, Chem. Phys. Lett. **444**, 232 (2007).
[54]T. C. Steimle, R. R. Bousquet, K.-I. C. Namiki, and A. J. Merer, J. Mol. Spectrosc. **215**, 10 (2002).
[55]T. C. Steimle, A. J. Marr, J. Xin, A. J. Merer, A. Athanassenas, and D. Gillett, J. Chem. Phys. **106**, 2060 (1997).
[56]R. Bousquet and T. C. Steimle, J. Chem. Phys. **114**, 1306 (2001).
[57]See supplementary material at http://dx.doi.org/10.1063/1.4803465 for Table S1.